ACS APPLIED MATERIALS & INTERFACES

www.acsami.org

Research Article

Printed, Wireless, Soft Bioelectronics and Deep Learning Algorithm for Smart Human−Machine Interfaces

Young-Tae Kwon,[⊥] Hojoong Kim,[⊥] Musa Mahmood, Yun-Soung Kim, Carl Demolder, and Woon-Hong Yeo*

Cite This: *ACS Appl. Mater. Interfaces* 2020, 12, 49398−49406

Read Online

ACCESS | Metrics & More | Article Recommendations | Supporting Information

ABSTRACT: Recent advances in flexible materials and wearable electronics offer a noninvasive, high-fidelity recording of biopotentials for portable healthcare, disease diagnosis, and machine interfaces. Current device-manufacturing methods, however, still heavily rely on the conventional cleanroom microfabrication that requires expensive, time-consuming, and complicated processes. Here, we introduce an additive nanomanufacturing technology that explores a contactless direct printing of aerosol nanomaterials and polymers to fabricate stretchable sensors and multilayered wearable electronics. Computational and experimental studies prove the mechanical flexibility and reliability of soft electronics, considering direct mounting to the deformable human skin with a curvilinear surface. The dry, skin-conformal graphene biosensor, without the use of conductive gels and aggressive tapes, offers an enhanced biopotential recording on the skin and multiple uses (over ten times) with consistent measurement of electromyograms. The combination of soft bioelectronics and deep learning algorithm allows classifying six classes of muscle activities with an accuracy of over 97%, which enables wireless, real-time, continuous control of external machines such as a robotic hand and a robotic arm. Collectively, the comprehensive study of nanomaterials, flexible mechanics, system integration, and machine learning shows the potential of the printed bioelectronics for portable, smart, and persistent human−machine interfaces.

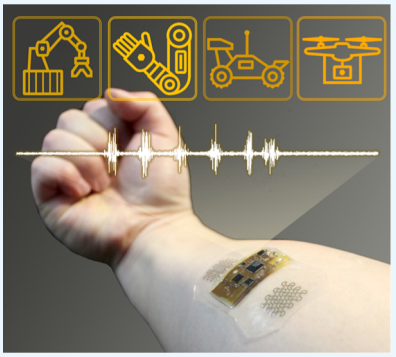

KEYWORDS: *additive nanomanufacturing, printed bioelectronics, deep learning algorithm, human−machine interface, electromyograms (EMGs)*

INTRODUCTION

Flexible and stretchable electronics have received significant attention as promising alternatives to conventional rigid electronics.[1−5] With advances in polymers and nanomaterials, many soft electronics have been developed for a wide range of bioelectronics, including personalized healthcare monitoring,[6−9] implantable biomedical devices,[10−12] and robotic control systems.[13−15] However, the practical route for manufacturing of such electronics still relies on cost-prohibitive, low-throughput fabrication processes that include photolithography, high-vacuum etching, and expensive thin-film deposition.[16,17] To overcome the challenges, recent developments in additive manufacturing of nanomaterials and solution-based material processing have demonstrated the capability to fabricate flexible, wearable devices. These methods have advantages of minimal material consumption, fast fabrication, and minimal use of equipment.[12,18] For bioelectronic applications, utilization of biocompatible nanomaterials is required because of the direct skin contact of sensors. Highly conductive nanomaterial inks, including silver (Ag) and copper (Cu), lead to low skin-to-electrode contact impedance, allowing the high-fidelity physiological recording from the human skin.[9,19−21] However, the direct contact of printed metals with highly corrosive and oxidizing properties to the skin could cause adverse health effects and degradation of signal quality.[22] For example, Ag ions that are released from the printed Ag sensor interact with membrane tissues and activate the signaling pathway, resulting in an inhibition of cell proliferation.[23,24] Thus, new biocompatible nanomaterials are required to manufacture biosensors that can be safely mounted on the skin for continuous monitoring of biopotentials.

Here, we introduce a fully printed, nanostructured, soft bioelectronic system that is made of graphene via additive manufacturing. Aerosol jet printing (AJP) of nanomaterials and polymers enables a high-throughput, efficient, and rapid fabrication of nanomembrane sensors and electronic platforms. The graphene nanomaterial conserves the intrinsic electrical and morphological characteristics while offering excellent cell biocompatibility and high-quality recording of biopotentials on the skin. The fully integrated, wearable bioelectronic system, including nanomembrane sensors and wireless flexible circuits,

Received: August 6, 2020
Accepted: October 9, 2020
Published: October 21, 2020

https://dx.doi.org/10.1021/acsami.0c14193
ACS Appl. Mater. Interfaces 2020, 12, 49398−49406

Table 1. Comparison of Fabrication Methods for Biosensors and Circuit Systems

reference	fabrication method	sensor material	sensor function	circuit material	circuit function
this work	all printed (both sensor and circuit)	graphene/PI on elastomer	EMG detection	PI/graphene/Ag/PI/Ag/PI on elastomer (multi-layered structure)	wireless data acquisition via Bluetooth
27	laser-ablation (sensor) printing and etching (circuit)	eutectic gallium indium on elastomer	EMG detection	Cu on elastomer (single layer)	wireless data acquisition via Bluetooth
28	transfer printing (sensor)	CVD-grown graphene[a] on medical tape	ECG detection		
29	printed (sensor)	PEDOT:PSS/Ag on PEN	temperature detection	rigid circuit board (single layer)	
30	printed (sensor)	Ag-In-Ga on textile	EMG detection		wireless data acquisition via Bluetooth
31	microfabrication (sensor)	Au/Cr on adhesive silicone	EMG detection		
32	printed trace	eutectic gallium indium—Ag			

[a]CVD: chemical vapor deposition.

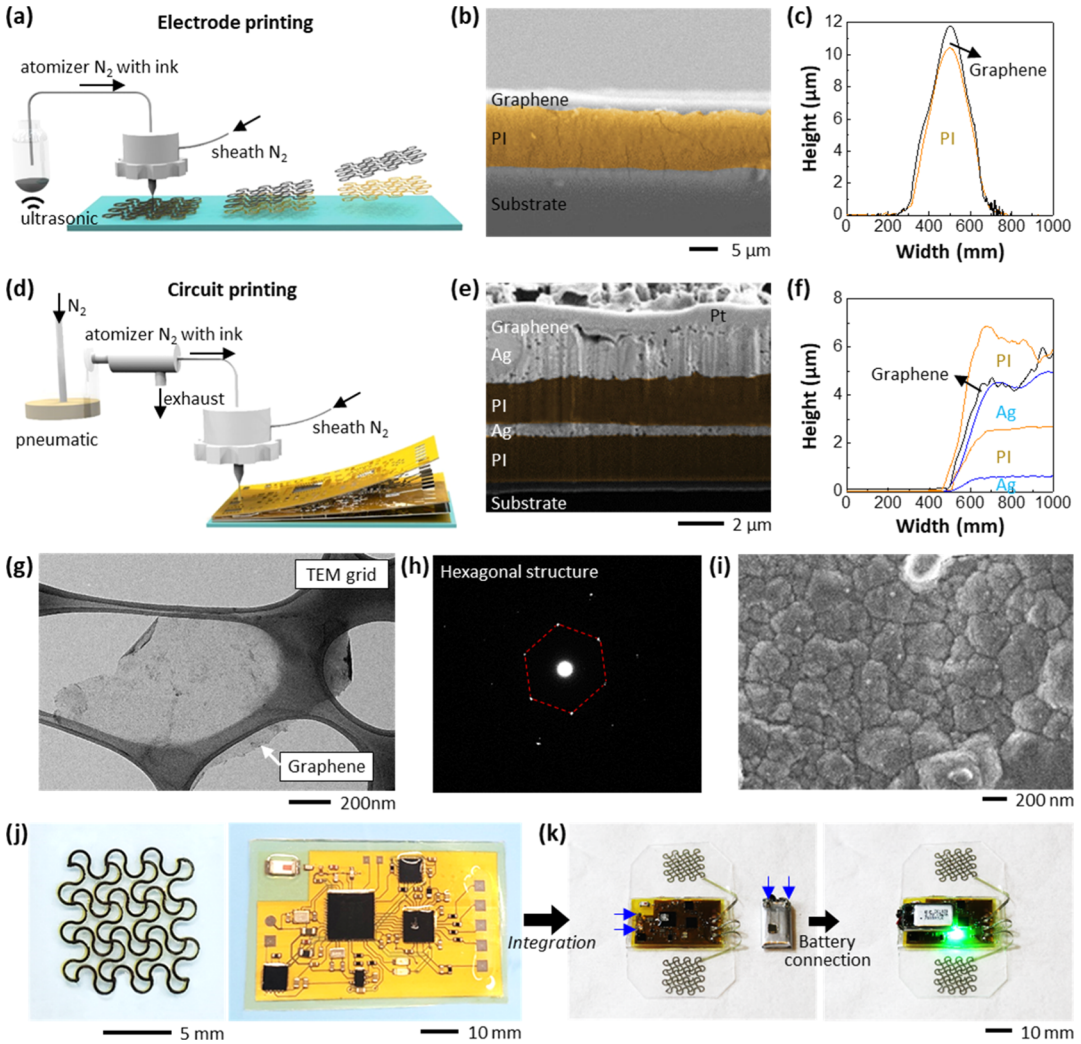

Figure 1. Nanomanufacturing and material characterization. (a) Illustration of printing of nanomaterials to fabricate a nanomembrane electrode. This printing uses an ultrasonic atomizer for low viscous ink. (b) Cross-sectional SEM image showing a multilayered sensor structure, including graphene, PI, and elastomer substrate. (c) Measured cross-sectional profile of the printed sensor in (b). (d) Illustration of printing of nanomaterials to fabricate circuit interconnects. This process uses a pneumatic atomizer for a high viscous ink. (e) FIB-assisted SEM image showing the printed, multilayered circuit that is composed of the graphene, Ag, PI, and elastomer membrane. (f) Profile graph of the printed circuit on the substrate. (g) TEM image of graphene. (h) Electron diffraction pattern showing the single crystalline of the six-fold symmetry of the hexagonal structure (guided by a dotted red line). (i) SEM image of the printed Ag pattern after photonic sintering. (j) Close-up photographs of the printed electrode (left) and circuit with functional chips (right) on elastomeric membranes. (k) Photographs showing the integrated, all-in-one system before (left) and after (right) battery connection. The battery is easily attached, facilitated by the small magnets (blue arrows).

https://dx.doi.org/10.1021/acsami.0c14193
ACS Appl. Mater. Interfaces 2020, 12, 49398−49406

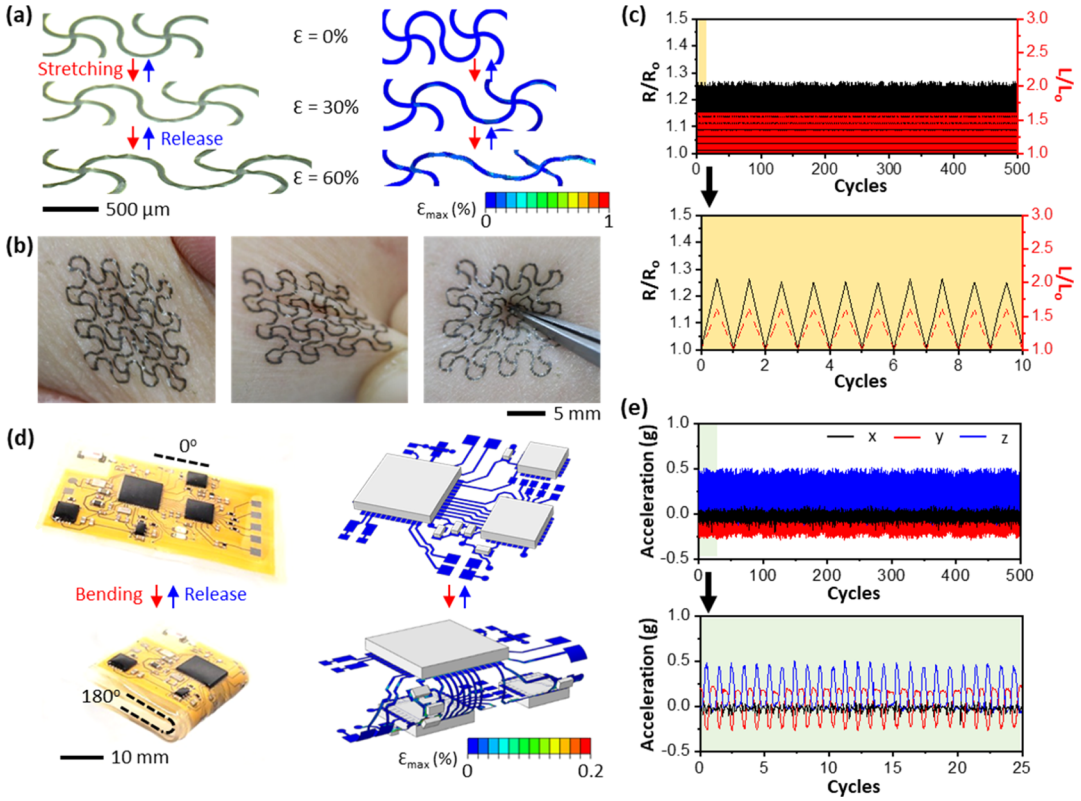

Figure 2. Mechanical behaviors of printed electrodes and circuits. (a) Open-mesh structured electrode showing stretchability up to 60%—(left) fabricated electrode and (right) FEA results. (b) Series of optical images of a printed electrode on the skin, going through compression, pinching, and poking. (c) Relative resistance change in an electrode upon cyclic 60% stretching for 500 times. The graph representing relative resistance change (black) according to strain change (red). The bottom chart reveals the first 10 stretching cycles. (d) Printed circuit with applied bending up to 180° (left), along with FEA results showing a similar behavior. (e) Three-axis acceleration data during 500 cyclic bendings, indicating that the device could maintain its power connectivity and operation without failure. The bottom data show the first 25 bending cycles.

demonstrates accurate monitoring of the electromyograms (EMGs) on the skin. We also develop a deep learning algorithm based on convolutional neural networks (CNNs) to classify the measured EMG signals from different muscle activities. The combination of the bioelectronics and machine learning demonstrates real-time, wireless control of external machines as an example of Smart HMI.

RESULTS AND DISCUSSION

Nanomanufacturing, Material Characterization, and System Integration. In this work, we developed a new nanomanufacturing method that used multiple nanomaterials, including graphene, Ag, and polyimide (PI), to fabricate stretchable sensors and electronics. Among them, in the previous study,[25,26] the graphene ink shows the stable structural quality and high electrical properties for the sensor development. Table 1 shows the summary of recently developed fabrication methods for biosensors and circuit systems,[27−32] which captures the main contribution of our approach in the development of all-printed bioelectronics. Figure 1 summarizes the nanomanufacturing process, characterized materials, and strategies of integrated bioelectronics. The AJP process allows a wide range of viscosity, from 1 to 1000 cP, to directly print various types of micropatterns via two atomizing modes of ultrasonic and pneumatic.[33,34] The ultrasonic atomization generates aerosol jet droplets of less than 50 nm in diameter, which has a limited viscosity range from 1 to 30 cP.[35] In contrast, the pneumatic atomization can eject atomized inks with a larger viscosity range of 1 to 1000 cP because the high-velocity gas stream is capable of transporting the particles up to 500 nm in size.[35] Details of the printing conditions and ink preparation are summarized in Table S1.

Figure 1a illustrates the additive manufacturing of a stretchable nanomembrane electrode via ultrasonic atomization of graphene ink (top layer) and PI ink (bottom supporting layer). Figure 1b,c captures the fabricated electrode, made of 10 μm-thick PI and 1 μm-thick conductive graphene on a soft elastomeric membrane. Figure 1d shows the fabrication process of flexible circuit interconnects with multiple layers. The scanning electron microscopy (SEM) image in Figure 1e and the profile image in Figure 1f show the details of the circuit structure, including 2 μm-thick base PI, 0.4 μm-thick Ag, 2 μm-thick middle PI, 1.9 μm-thick Ag, 0.1 μm-thick graphene, and 1.2 μm-thick final PI. Within the multilayered structure, the middle PI layer works as an electrical insulator between the first and second Ag layers except for the circular contact VIAs. The details of step-by-step fabrication procedures appear in Figure S1.

For the design of wearable biosensors, the core material must have two essential properties (details of the structural design in Figure S2): one is biocompatibility for the direct contact to the skin and the other is high conductivity for electrical sensing. In this study, we employ the selectively edge-oxidized graphene nanomaterial, prepared based on the prior report.[25] The atomic electron microscopy (AFM) and measured size histograms in Figure S3 capture that the

https://dx.doi.org/10.1021/acsami.0c14193
ACS Appl. Mater. Interfaces 2020, 12, 49398−49406

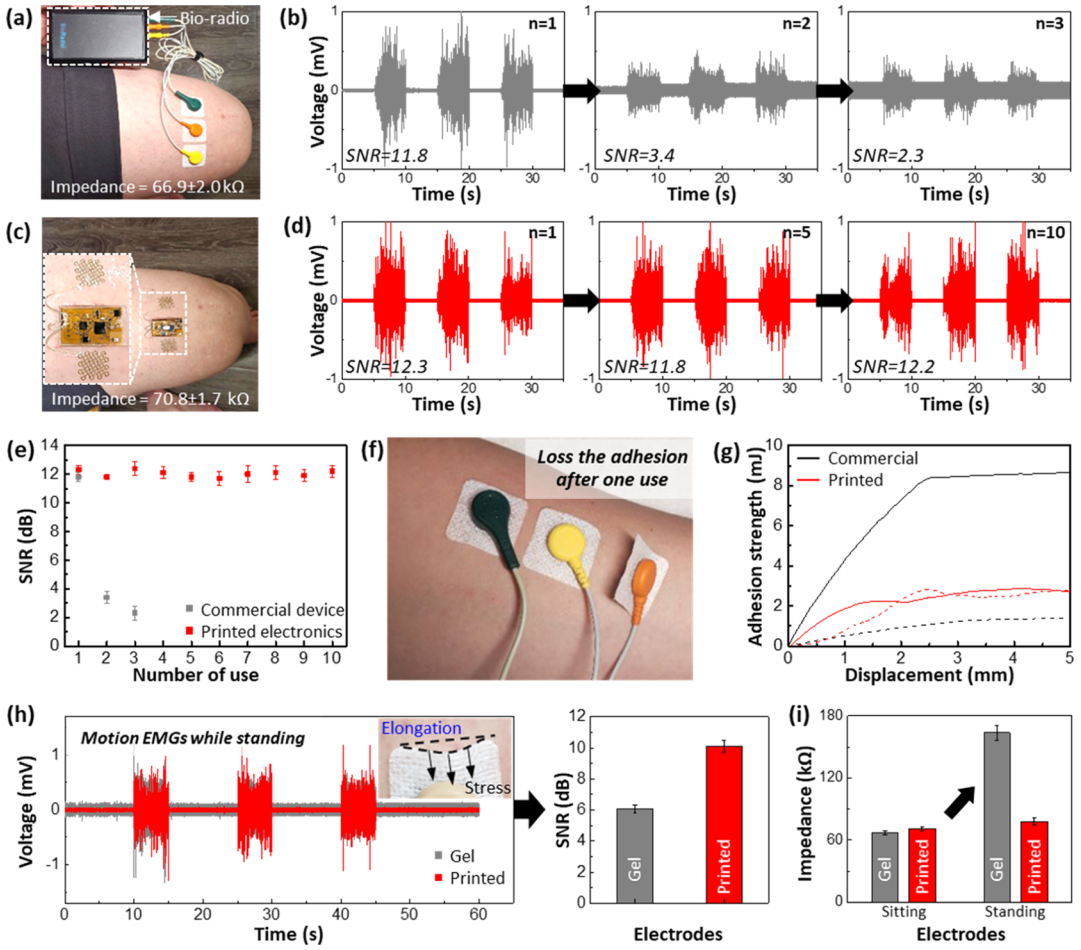

Figure 3. Comparison of the device performance in EMG recording. (a) Photograph of a commercial device (BioRadio) mounted on the skin. The skin-electrode contact impedance is 66.9 ± 2.0 kΩ (n = 5). (b) EMG signals and SNR data from the commercial gel electrodes during the leg flexion via multiple mountings and removals up to three times, showing significant reduction after three trials. (c) Photograph of a soft electronic system on the skin. Inset is a high-resolution image of the mounted printed device. (d) Reusability demonstration of the soft electronics up to 10 uses, showing a negligible change in the EMG SNR. (e) Summarized graph capturing the SNR comparison between the commercial device and printed electronics. The gel electrodes show no signal after the third use. Error bars show standard deviations from three EMG recordings (n = 3). (f) Photograph revealing the loss of adhesion of the gel electrode after the third use. (g) Adhesion comparison of the commercial device and soft electronics after multiple uses (solid line: first use, dotted line: last use). The adhesive of gel electrodes is significantly reduced after three uses. (h) Simultaneous comparison of measured EMG signals between the gel and printed electrodes during a subject's leg flexion while standing. The inset photograph indicates significantly elongated skin by the applied stress from the rigid and heavy electrode, resulting in a lower SNR than the printed one. (i) Comparison of impedance values between the gel and the printed electrodes while sitting and standing where the higher impedance for the gel electrode is caused by fluctuation and slight detachment of the rigid sensor from the skin.

synthesized graphene is 3.6 nm thick with 2 μm in lateral size, which indicates the high aspect ratio. In addition, the transmission electron microscopy (TEM) image in Figure 1g shows a wide-dimension graphene sheet. As shown in Figure 1h, the selected area electron diffraction pattern reveals the single crystalline of the six-fold symmetry of the hexagonal structure, suggesting that the nature of graphene is well-preserved. Such a high-aspect-ratio graphene also exhibits excellent biocompatibility, proven by the cultured skin keratinocyte cells (Figure S4). As the cells are identified in a viability assay as dead (dyed in blue) or alive keratinocyte cells by fluorescence microscopy, the graphene nanomaterial shows the comparable cell viability to the control sample.

Another SEM investigation characterizes the printed Ag traces that work as conductive layers for the flexible circuit. Figure 1i shows highly dense, well-sintered Ag nanoparticles. The left photograph in Figure 1j shows a printed stretchable electrode based on graphene on top of PI, while another image on the right shows a fully integrated circuit that has mounted functional chips on the printed flexible circuit interconnects. The integrated electronic system is powered by a rechargeable lithium-ion polymer battery (40 mA h, DTP301120, Shenzhen Data Power Technology). The battery can be easily mounted on the electronics, facilitated by small neodymium magnets marked in Figure 1k (left). The green LED light indicates the secured connection (right, Figure 1k).

Mechanical Behaviors of Printed Electrodes and Circuits. Figure 2 summarizes a set of computational and experimental studies on the mechanical flexibility, stretchability, and reliability of the designed electrodes and circuits. The open-mesh patterned electrode is stretchable up to 60% under tensile strain because of the out-of-plane buckling without mechanical fracture (Figure 2a, left). The corresponding computational study using finite element analysis (FEA) supports the mechanical behavior upon excessive stretching (Figure 2a, right). Simulated 60% stretching of the electrode

https://dx.doi.org/10.1021/acsami.0c14193
ACS Appl. Mater. Interfaces 2020, 12, 49398−49406

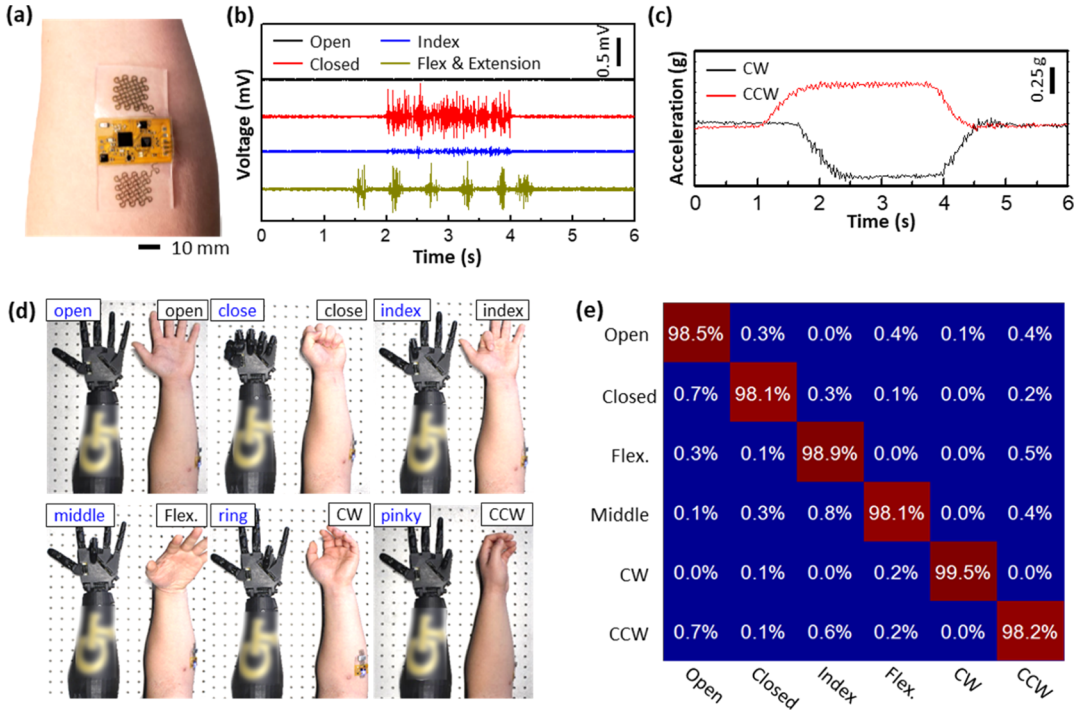

Figure 4. Demonstration of wireless, wearable bioelectronics for Smart HMI—control of a printed robotic hand. (a) Photograph of a fabricated bioelectronic system mounted on the forearm for the recording of EMG. (b) Representative EMG signals from four different gestures, including open hand (black), closed hand (red), index finger flexion (blue), and wrist flexion (green). (c) Representative acceleration data, measured from arm rotation clockwise (black) and counterclockwise (red) in the *z*-axis. (d) Demonstration of real-time, wireless control of six robotic hand motions via the subject's different gestures, including open hand, closed hand, index flexion, wrist flexion, and two arm rotations. (e) Summarized confusion matrix showing the classification accuracy of 98.5% with six classes.

shows the maximum principal strain of less than 1%. Based on the studied design criteria, we fabricated stretchable electrodes for direct mounting on the skin. Figure 2b shows a series of photographs of a skin-conformal nanomembrane electrode on the forearm, which endures compressing (left), pinching (middle), and pressing with a tweezer (right; Figure 2b). No structural fracture was observed when investigated using a microscope.

Considering a long-term, continuous use of the skin-wearable electrode, we conducted a cyclic loading mechanical test. The result in Figure 2c shows a negligible change in measured electrical resistance after 500 cycles with a 60% tensile strain, which proves the mechanical reliability. Additional studies of the printed flexible circuit in Figure 2d demonstrate the mechanical robustness upon excessive bending (180 degrees at 1.5 mm in the radius of the curvature). Both experimental and computational results indicate that the device experiences minimal mechanical stress during bending. Figure 2e summarizes the quantitative measure of the mechanical reliability via monitoring of acceleration sensor data during 500 cyclic bending, which shows a negligible change in the measured data. Overall, the collective results prove the mechanical stability and reliability of the device for direct integration with the skin and follow-up monitoring of biopotentials.

Comparison of the Device Performance in EMG Recording. In this study, we compared the printed bioelectronics with a clinical-grade commercial EMG system to validate the device performance. Figure 3a shows the commercial system (BioRadio, Great Lakes NeuroTechnologies) that requires three gel electrodes and a separate wireless data acquisition system. A subject wears the sensors on the upper leg and measures EMG signals with muscle flexion (details of gestures in Figure S5). Figure 3b captures the EMG data from the upper leg with the commercial system, showing significant degradation of signals from the initial electrode mounting to reuse three times: change in the signal-to-noise ratio (SNR) from 11.8 to 2.3. The SNR is calculated as[9,36]

$$\mathrm{SNR} = 10 \log_{10}\left[\left(\frac{A_{\mathrm{signal}}}{A_{\mathrm{noise}}}\right)^2\right] \quad (1)$$

where A_{signal} is the average full-wave rectified EMG recorded during gestures and A_{noise} is the average full-wave rectified EMG during rest.

In contrast, the printed soft electronics (Figure 3c) on the self-adhesive elastomer demonstrates consistent, high-quality recording of EMG data with 10 repetitive uses (Figure 3d), which captures maintained conformal lamination and adhesion of sensors to the skin. Figure 3e compares the measured SNR of two devices according to the number of uses. The major difference includes the device form factor, material stiffness, and substrate material. Specifically, the conventional electrode uses the aggressive acrylate tape that often exfoliates the stratum corneum when detached from the skin, which is why the gel electrode loses the adhesion (Figure 3f). On the other hand, the silicone elastomeric membrane of soft electronics offers gentle but adequate skin contact, allowing multiple uses with consistent adhesion. Figure 3g proves the difference between these materials by measuring adhesion strength. The peel force of the gel electrode (8.7 mJ, solid black line) is dramatically dropped to 1.1 mJ (black dotted line) after one

https://dx.doi.org/10.1021/acsami.0c14193
ACS Appl. Mater. Interfaces 2020, 12, 49398−49406

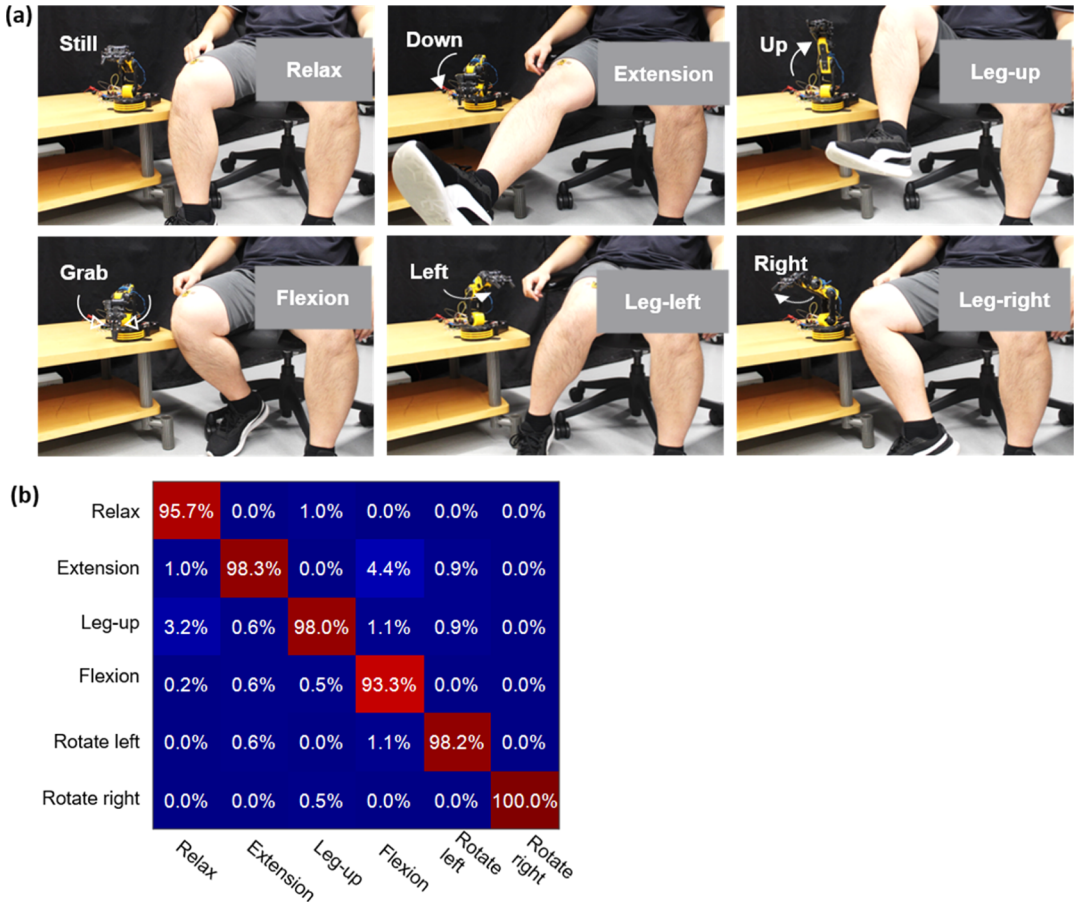

Figure 5. In vivo demonstration of wireless control of a robotic arm via leg EMG signals. (a) Series of photographs capturing six different motions of the robotic arm controlled by the leg gestures, including relax, extension, leg-up, flexion, leg-left, and leg-right. Details appear in Movie S1. (b) Summarized confusion matrix showing the classification accuracy of 97.3% across six classes shown in (a).

use, while the printed electrode maintains the adhesion (2.9 mJ, red line).

In addition, a simultaneous comparison of two devices with induced motion captures the advantage of the soft electrodes. As summarized in Figure 3h, the SNR value from the printed electrode is higher than that from the gel electrode. EMG data were measured by two different motions, including standing still and flexion of the leg (details in Figure S6). In this setting, the rigid and heavy electrode (>10 g) with the adhesive tape causes excessive stress on the skin, which elongates the outmost layer of the skin (inset in Figure 3h).[37] The measured impedance data in Figure 3i show that the soft electrode (0.1 g) has a negligible effect during sitting or standing. On the other hand, the weight of rigid gel electrodes causes an unfavorable increase in the contact impedance while standing. Collectively, this study shows that the soft, lightweight electrode is not only reusable but also reliable with minimized motion artifacts compared to the conventional electrode.

Demonstration of the Wireless, Wearable Bioelectronics for Smart HMI. This study demonstrates a successful application of the developed wireless bioelectronics and deep learning algorithm for Smart HMI. Specifically, noninvasive EMG signals and motion-based acceleration, measured on the skin, are used to have real-time, wireless control of external machines. Figure 4a shows an all-in-one bioelectronic system, mounted on the skin between the flexor carpi radialis and flexor carpi ulnaris of the forearm for the control of external devices.[38] A flowchart in Figure S7 describes the entire process of how the combination of wearable electronics and deep learning offers real-time machine control.

EMG and acceleration data recorded from the device are wirelessly transmitted to a tablet via Bluetooth, which undergoes signal processing in a custom-designed Android application. The data buffer for classification is updated as soon as a new packet is received. The final 0.512 s of data (128 data points) is processed and classified for every 10 packets received (60 data points or 0.240 s). The algorithm includes a safety buffer to avoid any unwanted error from the fast classification rate and the corresponding machine control; the final control command is delivered to the machine when all outputs match. For the classification of multiple EMG signals, we developed a deep learning algorithm, based on CNNs that could recognize subtle firing rate patterns while also considering the amplitude.[39] For preprocessing, data are screened using the third-order high-pass Butterworth filter at a cutoff frequency of 1 Hz. The *z*-axis acceleration data, measured from the forearm rotation, are implemented in the analysis using the onboard accelerometer in the bioelectronics.

Figure 4b,c shows the representative set of EMG and acceleration data measured using the wearable device on the forearm. A subject makes multiple motion gestures, including open hand, closed hand, index finger flexion, wrist flexion, and arm rotations clockwise and counterclockwise. Each of these gestures is utilized for real-time, wireless control of six motions (open hand, closed hand, and four different fingers) of a robotic hand, as shown in Figure 4d. Details of the list of

https://dx.doi.org/10.1021/acsami.0c14193
ACS Appl. Mater. Interfaces 2020, 12, 49398−49406

commands used in this work appear in Table S2a. Collectively, the experimental study captures the high performance of a single-channel wearable device, showing great classification accuracy of 98.5% with six classes and over ten trials (Figure 4e).

Figure 5 summarizes the experimental result showing another example of Smart HMI, suggesting that the wearable electronics can record EMG from other parts of the body. The wearable, single-channel bioelectronics is mounted on the upper leg, specifically on the vastus intermedius muscle to measure EMG from different gestures. Figure S8 shows the data acquisition, processing, and transmission process to control a miniaturized industrial robotic arm. This work also uses two types of physiological data, including leg EMG and acceleration, classified by the developed CNN algorithm. Figure 5a summarizes the machine control commands with six motions, including relaxation (no movement), leg extension, leg-up motion, flexion, and leg rotations (to the left and right). Real-time control of the robotic arm via the leg EMG appears in Movie S1. Details of the control commands appear in Table S2b, while Figure S9 shows a set of raw EMG data measured from the vastus intermedius muscle. The classification accuracy with six classes over ten trials shows 97.3% in real-time, wireless control of the miniaturized robotic arm (Figure 5b). To further improve the accuracy, future work will focus on adding more channels in the sensor system and optimizing the classification algorithm.

CONCLUSIONS

This paper reports a new class of advanced technologies in nanomaterial processing, additive manufacturing, and machine learning, enabling real-time, wireless, and Smart HMI. The ultrathin, lightweight, soft electronics that include nanomembrane sensors and thin-film circuits allow for conformal skin contact, comfortable wear, and multiple reusabilities with reduced motion artifacts in the physiological signal recording. A set of computational and experimental studies validate the mechanical safety and reliability of the wearable device to endure multimodal deformation in various application cases. The combination of skin-conformal bioelectronics and deep learning CNN enables the highly accurate classification of six motion classes: 98.5 and 97.3% for controlling a robotic hand and a miniaturized industrial arm, respectively. The fully printed, all-in-one soft electronics presented in this work will serve as an advanced intelligent system for areas of smart rehabilitation, closed-loop prosthesis, disease diagnosis, and persistent machine interfaces.

EXPERIMENTAL SECTION

Preparation for PI, Graphene, and Ag Inks. The PI ink was prepared by the mixture of a precursor (PI-2545, DuPont) and solvent (1-methyl-2-pyrrolidineone; Sigma-Aldrich) in a 4:1 ratio. For the synthesis of graphene ink, we conducted the electrochemical process reported in our previous research.[25] A direct voltage of 10 V was applied between the graphite (Alfa Aesar) and Pt foil in an electrolyte solution, which is composed of ammonium sulfate (99%, Sigma-Aldrich) of 0.1 M and deionized (DI) water. After exfoliation, the as-synthesized graphene was purified using DI water to remove the residuals. The filtered wet graphene powder was dispersed in DI water and controlled to a concentration of 1%. Ag nanoparticle ink (Ag50XL, UT Dots) was mixed with xylene (*m*-xylene, Sigma-Aldrich) to prepare the concentration of 20%.[12]

Electrode Printing. The additive process was performed using the AJP method (Aerosol Jet 200, Optomec), and the optimized conditions are indicated in Table S1. A sacrificial layer of polymethyl methacrylate (PMMA) (950 PMMA, Kayaku Advanced Materials) was coated on a glass slide using a spin coater with the conditions of 1000 rpm and 30 s. Then, the coated PMMA was baked at 200 °C for 2 min. A PI ink is deposited using a 300 μm-diameter nozzle and cured at 250 °C for 1 h. The print head assembled with a 200 μm-diameter nozzle was precisely aligned to print the graphene ink. The printed graphene traces were thermally dried at 100 °C for 1 h. The elastomer membrane was prepared by mixing 5 g of 1:1 Ecoflex 00-30 (Smooth-On) and 5 g of 1:1 Ecoflex Gel (Smooth-On). The elastomer mixture was poured into a polystyrene dish (FB0875714, Fisher Scientific) and cured overnight. For the electrode transfer printing, the PMMA of the printed electrode was dissolved in an acetone bath overnight. PMMA works as a sacrificial layer to retrieve the electrode from the carrying substrate. Afterward, a water-soluble tape was used to pick up the electrode. Finally, the electrode was transfer-printed onto a 500 μm-thick elastomeric membrane (Figure S1c).

Circuit Printing. A PI ink was spin-coated on a PMMA/glass substrate at 2000 rpm for 60 s. First, Ag ink was deposited onto the PI layer using a 200 μm-diameter nozzle. The printed Ag was sintered with an intense pulsed light equipment (S-2200, XENON Corp.) under the optimal condition that is 2 kV/2 ms/5 times, for power and the number of pulses, respectively. The PI ink for the dielectric layer was printed and cured on the first Ag layer via the same parameters described previously. The second Ag layer was printed and photonic-sintered under identical conditions. The graphene ink was printed and dried at 100 °C for 1 h. The final PI layer for the encapsulation was printed and thermally cured at 250 °C for 1 h. The PMMA layer is removed using acetone to transfer the printed circuit onto the elastomer substrate. After transferring the printed circuit, the integration process was followed.

Integration with Chip Components. Solder paste (an alloy of Sn/Bi/Ag (42/57.6/0.4%), Chip Quik Inc.) was screen-printed with a stainless-steel stencil on the top surface of the circuit. The chip components, including the Bluetooth, voltage regulator, resistors, inductors, and capacitors, were mounted and reflowed by the heat treatment according to the temperature recommended by the solder paste manufacturer. The firmware of the Bluetooth-microcontroller was updated on the soldered circuit. The chip integration process followed the previously reported study.[25]

Characterization of Materials. Cross-sectional SEM images were taken by SEM combined with a focused ion beam (FIB-SEM; Nova Nanolab 200, FEI). The microscopy structures were investigated by TEM (JEM-2100F, JEOL) and AFM (XE-100, Park systems). A profilometer (Dektak 150, Veeco) was used for measuring the thickness of each printed layer. All mechanics were measured using a digital force gauge (M5-5, Mark-10) fixed on a motorized test stand (ESM303, Mark-10).

Study of FEA. The mechanical behavior was determined using ABAQUS software (Dassault Systemes Simulia Corporation, Johnston, RI). The simulation study focused on the mechanical reliability of the multilayered devices upon repetitive bending and stretching. For the computational modeling, the following parameters were used: Young's modulus (E) and Poisson's ratio (ν): E_{PI} = 2.5 GPa and ν_{PI} = 0.34 for PI; E_{Ag} = 40 GPa and ν_{Ag} = 0.37 for Ag.[40]

Study with Human Subjects. The study involved two volunteers aged between 18 and 40 and was conducted by following the approved IRB protocol (#H17212) at the Georgia Institute of Technology. Before the study, all subjects agreed with the study procedures and provided signed consent forms. For the device performance validation, we compared the printed electronics with a commercial device (BioRadio). For data acquisition, we use both devices with the following steps; both devices were placed on the forearm of a subject. We measured EMG data during resting (10 s) and closed hand (10 s) five times. After 100 s, we removed and remounted those devices in the same position, and the subject performed the same activities to compare the signal variation.

https://dx.doi.org/10.1021/acsami.0c14193
ACS Appl. Mater. Interfaces 2020, 12, 49398−49406

■ ASSOCIATED CONTENT

Supporting Information

The Supporting Information is available free of charge at https://pubs.acs.org/doi/10.1021/acsami.0c14193.

Fabrication of sensors and electronics; schematic illustration of multilayered printed bioelectronics; characterization of graphene dispersed in aqueous ink; biocompatibility study of printed electrodes; human leg gestures mounted with the commercial device and the soft electronics while sitting; human leg gestures mounted with the commercial device and the printed electronics at the same time while standing; flowchart showing the process of controlling a robot hand; flowchart showing the process of controlling a robotic arm; EMG and acceleration data from the human leg gestures; parameters for ink materials, printing, curing, and sintering; and list of commands for controlling external machines (PDF)

Real-time control of a robotic arm via EMG signals from the upper leg (MP4)

■ AUTHOR INFORMATION

Corresponding Author

Woon-Hong Yeo − *George W. Woodruff School of Mechanical Engineering, Institute for Electronics and Nanotechnology, Wallace H. Coulter Department of Biomedical Engineering, Parker H. Petit Institute for Bioengineering and Biosciences, and Center for Human-Centric Interfaces and Engineering, Neural Engineering Center, Institute for Materials, Institute for Robotics and Intelligent Machines, Georgia Institute of Technology, Atlanta, Georgia 30332, United States;* orcid.org/0000-0002-5526-3882; Email: whyeo@gatech.edu

Authors

Young-Tae Kwon − *George W. Woodruff School of Mechanical Engineering, Institute for Electronics and Nanotechnology, Georgia Institute of Technology, Atlanta, Georgia 30332, United States*

Hojoong Kim − *George W. Woodruff School of Mechanical Engineering, Institute for Electronics and Nanotechnology, Georgia Institute of Technology, Atlanta, Georgia 30332, United States*

Musa Mahmood − *George W. Woodruff School of Mechanical Engineering, Institute for Electronics and Nanotechnology, Georgia Institute of Technology, Atlanta, Georgia 30332, United States*

Yun-Soung Kim − *George W. Woodruff School of Mechanical Engineering, Institute for Electronics and Nanotechnology, Georgia Institute of Technology, Atlanta, Georgia 30332, United States*

Carl Demolder − *George W. Woodruff School of Mechanical Engineering, Institute for Electronics and Nanotechnology, Georgia Institute of Technology, Atlanta, Georgia 30332, United States*

Complete contact information is available at: https://pubs.acs.org/10.1021/acsami.0c14193

Author Contributions

[⊥]Y.-T.K. and H.K. contributed equally to this work. Y.-T.K. and W.-H.Y. conceived and designed the research; Y.-T.K., H.K., M.M., Y.-S.K., and C.D. performed the experiment and analyzed the data; and Y.-T.K., H.K., and W.-H.Y. wrote the paper.

Notes

The authors declare no competing financial interest.

■ ACKNOWLEDGMENTS

We acknowledge the support by the Georgia Research Alliance based in Atlanta, Georgia. This work was partially supported by the National Science Foundation (grant NRI-2024742) and the Georgia Tech IEN Seed Grant. Electronic devices in this work were fabricated at the Institute for Electronics and Nanotechnology, a member of the National Nanotechnology Coordinated Infrastructure, which is supported by the National Science Foundation (grant ECCS-2025462).

■ REFERENCES

(1) Kim, D.-H.; Lu, N.; Ma, R.; Kim, Y.-S.; Kim, R.-H.; Wang, S.; Wu, J.; Won, S. M.; Tao, H.; Islam, A.; Yu, K. J.; Kim, T.-i.; Chowdhury, R.; Ying, M.; Xu, L.; Li, M.; Chung, H.-J.; Keum, H.; McCormick, M.; Liu, P.; Zhang, Y.-W.; Omenetto, F. G.; Huang, Y.; Coleman, T.; Rogers, J. A. Epidermal Electronics. *Science* **2011**, *333*, 838−843.

(2) Kaltenbrunner, M.; Sekitani, T.; Reeder, J.; Yokota, T.; Kuribara, K.; Tokuhara, T.; Drack, M.; Schwödiauer, R.; Graz, I.; Bauer-Gogonea, S.; Bauer, S.; Someya, T. An Ultra-Lightweight Design for Imperceptible Plastic Electronics. *Nature* **2013**, *499*, 458−463.

(3) Xu, S.; Zhang, Y.; Jia, L.; Mathewson, K. E.; Jang, K.-I.; Kim, J.; Fu, H.; Huang, X.; Chava, P.; Wang, R.; Bhole, S.; Wang, L.; Na, Y. J.; Guan, Y.; Flavin, M.; Han, Z.; Huang, Y.; Rogers, J. A. Soft Microfluidic Assemblies of Sensors, Circuits, and Radios for the Skin. *Science* **2014**, *344*, 70−74.

(4) Lim, H. R.; Kim, H. S.; Qazi, R.; Kwon, Y. T.; Jeong, J. W.; Yeo, W. H. Advanced Soft Materials, Sensor Integrations, and Applications of Wearable Flexible Hybrid Electronics in Healthcare, Energy, and Environment. *Adv. Mater.* **2020**, *32*, 1901924.

(5) Herbert, R.; Kim, J.-H.; Kim, Y.; Lee, H.; Yeo, W.-H. Soft Material-Enabled, Flexible Hybrid Electronics for Medicine, Healthcare, and Human-Machine Interfaces. *Materials* **2018**, *11*, 187.

(6) Imani, S.; Bandodkar, A. J.; Mohan, A. V.; Kumar, R.; Yu, S.; Wang, J.; Mercier, P. P. A Wearable Chemical−Electrophysiological Hybrid Biosensing System for Real-Time Health and Fitness Monitoring. *Nat. Commun.* **2016**, *7*, 11650.

(7) Schwartz, G.; Tee, B. C.-K.; Mei, J.; Appleton, A. L.; Kim, D. H.; Wang, H.; Bao, Z. Flexible Polymer Transistors with High Pressure Sensitivity for Application in Electronic Skin and Health Monitoring. *Nat. Commun.* **2013**, *4*, 1859.

(8) Park, M.; Do, K.; Kim, J.; Son, D.; Koo, J. H.; Park, J.; Song, J.-K.; Kim, J. H.; Lee, M.; Hyeon, T.; Kim, D.-H. Oxide Nanomembrane Hybrids with Enhanced Mechano- and Thermo-Sensitivity for Semitransparent Epidermal Electronics. *Adv. Healthcare Mater.* **2015**, *4*, 992−997.

(9) Kwon, Y.-T.; Kim, Y.-S.; Lee, Y.; Kwon, S.; Lim, M.; Song, Y.; Choa, Y.-H.; Yeo, W.-H. Ultrahigh Conductivity and Superior Interfacial Adhesion of a Nanostructured, Photonic-Sintered Copper Membrane for Printed Flexible Hybrid Electronics. *ACS Appl. Mater. Interfaces* **2018**, *10*, 44071−44079.

(10) Ma, Y.; Zheng, Q.; Liu, Y.; Shi, B.; Xue, X.; Ji, W.; Liu, Z.; Jin, Y.; Zou, Y.; An, Z.; Zhang, W.; Wang, X.; Jiang, W.; Xu, Z.; Wang, Z. L.; Li, Z.; Zhang, H. Self-Powered, One-Stop, and Multifunctional Implantable Triboelectric Active Sensor for Real-Time Biomedical Monitoring. *Nano Lett.* **2016**, *16*, 6042−6051.

(11) Kang, S.-K.; Murphy, R. K. J.; Hwang, S.-W.; Lee, S. M.; Harburg, D. V.; Krueger, N. A.; Shin, J.; Gamble, P.; Cheng, H.; Yu, S. Bioresorbable Silicon Electronic Sensors for the Brain. *Nature* **2016**, *530*, 71−76.

(12) Herbert, R.; Mishra, S.; Lim, H. R.; Yoo, H.; Yeo, W. H. Fully Printed, Wireless, Stretchable Implantable Biosystem toward Battery-

less, Real-Time Monitoring of Cerebral Aneurysm Hemodynamics. *Adv. Sci.* **2019**, *6*, 1901034.
(13) Chen, S.; Jiang, J.; Xu, F.; Gong, S. Crepe Cellulose Paper and Nitrocellulose Membrane-Based Triboelectric Nanogenerators for Energy Harvesting and Self-Powered Human-Machine Interaction. *Nano Energy* **2019**, *61*, 69−77.
(14) Zhang, B.; Tang, Y.; Dai, R.; Wang, H.; Sun, X.; Qin, C.; Pan, Z.; Liang, E.; Mao, Y. Breath-based human-machine interaction system using triboelectric nanogenerator. *Nano Energy* **2019**, *64*, 103953.
(15) Jeong, J.-W.; Yeo, W.-H.; Akhtar, A.; Norton, J. J. S.; Kwack, Y.-J.; Li, S.; Jung, S.-Y.; Su, Y.; Lee, W.; Xia, J.; Cheng, H.; Huang, Y.; Choi, W.-S.; Bretl, T.; Rogers, J. A. Materials and Optimized Designs for Human-Machine Interfaces Via Epidermal Electronics. *Adv. Mater.* **2013**, *25*, 6839−6846.
(16) Lee, Y.-I.; Kim, S.; Jung, S.-B.; Myung, N. V.; Choa, Y.-H. Enhanced Electrical and Mechanical Properties of Silver Nanoplatelet-Based Conductive Features Direct Printed on a Flexible Substrate. *ACS Appl. Mater. Interfaces* **2013**, *5*, 5908−5913.
(17) Kwon, Y.-T.; Lee, Y.-I.; Kim, S.; Lee, K.-J.; Choa, Y.-H. Full Densification of Inkjet-Printed Copper Conductive Tracks on a Flexible Substrate Utilizing a Hydrogen Plasma Sintering. *Appl. Surf. Sci.* **2017**, *396*, 1239−1244.
(18) Herbert, R.; Lim, H.-R.; Yeo, W.-H. Printed, Soft, Nanostructured Strain Sensors for Monitoring of Structural Health and Human Physiology. *ACS Appl. Mater. Interfaces* **2020**, *12*, 25020.
(19) Matsuhisa, N.; Inoue, D.; Zalar, P.; Jin, H.; Matsuba, Y.; Itoh, A.; Yokota, T.; Hashizume, D.; Someya, T. Printable Elastic Conductors by in Situ Formation of Silver Nanoparticles from Silver Flakes. *Nat. Mater.* **2017**, *16*, 834−840.
(20) Park, M.; Im, J.; Shin, M.; Min, Y.; Park, J.; Cho, H.; Park, S.; Shim, M.-B.; Jeon, S.; Chung, D.-Y.; Bae, J.; Park, J.; Jeong, U.; Kim, K. Highly Stretchable Electric Circuits from a Composite Material of Silver Nanoparticles and Elastomeric Fibres. *Nat. Nanotechnol.* **2012**, *7*, 803.
(21) Mishra, S.; Kim, Y.-S.; Intarasirisawat, J.; Kwon, Y.-T.; Lee, Y.; Mahmood, M.; Lim, H.-R.; Herbert, R.; Yu, K. J.; Ang, C. S.; Yeo, W.-H. Soft, Wireless Periocular Wearable Electronics for Real-Time Detection of Eye Vergence in a Virtual Reality toward Mobile Eye Therapies. *Sci. Adv.* **2020**, *6*, No. eaay1729.
(22) Choi, S.; Han, S. I.; Jung, D.; Hwang, H. J.; Lim, C.; Bae, S.; Park, O. K.; Tschabrunn, C. M.; Lee, M.; Bae, S. Y.; Yu, J. W.; Ryu, J. H.; Lee, S.-W.; Park, K.; Kang, P. M.; Lee, W. B.; Nezafat, R.; Hyeon, T.; Kim, D.-H. Highly conductive, stretchable and biocompatible Ag-Au core-sheath nanowire composite for wearable and implantable bioelectronics. *Nat. Nanotechnol.* **2018**, *13*, 1048−1056.
(23) McShan, D.; Ray, P. C.; Yu, H. Molecular Toxicity Mechanism of Nanosilver. *J. Food Drug Anal.* **2014**, *22*, 116−127.
(24) Levard, C.; Hotze, E. M.; Lowry, G. V.; Brown, G. E., Jr Environmental Transformations of Silver Nanoparticles: Impact on Stability and Toxicity. *Environ. Sci. Technol.* **2012**, *46*, 6900−6914.
(25) Baek, S.; Kim, J.; Kim, H.; Park, S.; Ban, H. W.; Gu, D. H.; Jeong, H.; Kim, F.; Lee, J.; Jung, B. M.; Choa, Y.-H.; Kim, K. H.; Son, J. S. Controlled Grafting of Colloidal Nanoparticles on Graphene through Tailored Electrostatic Interaction. *ACS Appl. Mater. Interfaces* **2019**, *11*, 11824−11833.
(26) Kwon, Y.-T.; Kim, Y.-S.; Kwon, S.; Mahmood, M.; Lim, H.-R.; Park, S.-W.; Kang, S.-O.; Choi, J. J.; Herbert, R.; Jang, Y. C. All-Printed Nanomembrane Wireless Bioelectronics Using a Biocompatible Solderable Graphene for Multimodal Human-Machine Interfaces. *Nat. Commun.* **2020**, *11*, 3450.
(27) Marques, D. G.; Lopes, P. A.; de Almeida, A. T.; Majidi, C.; Tavakoli, M. Reliable Interfaces for Egain Multi-Layer Stretchable Circuits and Microelectronics. *Lab Chip* **2019**, *19*, 897−906.
(28) Kabiri Ameri, S.; Ho, R.; Jang, H.; Tao, L.; Wang, Y.; Wang, L.; Schnyer, D. M.; Akinwande, D.; Lu, N. Graphene Electronic Tattoo Sensors. *ACS Nano* **2017**, *11*, 7634−7641.
(29) Wang, Y.-F.; Sekine, T.; Takeda, Y.; Yokosawa, K.; Matsui, H.; Kumaki, D.; Shiba, T.; Nishikawa, T.; Tokito, S. Fully Printed Pedot:Pss-Based Temperature Sensor with High Humidity Stability for Wireless Healthcare Monitoring. *Sci. Rep.* **2020**, *10*, 2467.
(30) Lopes, P. A.; Paisana, H.; De Almeida, A. T.; Majidi, C.; Tavakoli, M. Hydroprinted Electronics: Ultrathin Stretchable Ag-In-Ga E-Skin for Bioelectronics and Human-Machine Interaction. *ACS Appl. Mater. Interfaces* **2018**, *10*, 38760−38768.
(31) Tian, L.; Zimmerman, B.; Akhtar, A.; Yu, K. J.; Moore, M.; Wu, J.; Larsen, R. J.; Lee, J. W.; Li, J.; Liu, Y.; Metzger, B.; Qu, S.; Guo, X.; Mathewson, K. E.; Fan, J. A.; Cornman, J.; Fatina, M.; Xie, Z.; Ma, Y.; Zhang, J.; Zhang, Y.; Dolcos, F.; Fabiani, M.; Gratton, G.; Bretl, T.; Hargrove, L. J.; Braun, P. V.; Huang, Y.; Rogers, J. A. Large-Area Mri-Compatible Epidermal Electronic Interfaces for Prosthetic Control and Cognitive Monitoring. *Nat. Biomed. Eng.* **2019**, *3*, 194−205.
(32) Tavakoli, M.; Malakooti, M. H.; Paisana, H.; Ohm, Y.; Green Marques, D.; Alhais Lopes, P.; Piedade, A. P.; de Almeida, A. T.; Majidi, C. EGaIn-Assisted Room-Temperature Sintering of Silver Nanoparticles for Stretchable, Inkjet-Printed, Thin-Film Electronics. *Adv. Mater.* **2018**, *30*, 1801852.
(33) Salary, R. R.; Lombardi, III, J. P.; Weerawarne, D. L.; Rao, P. K.; Poliks, M. D. A State-of-the-Art Review on Aerosol Jet Printing (Ajp) Additive Manufacturing Process. *International Manufacturing Science and Engineering Conference*; American Society of Mechanical Engineers, 2019; p V001T01A035.
(34) Stoukatch, S.; Laurent, P.; Dricot, S.; Axisa, F.; Seronveaux, L.; Vandormael, D.; Beeckman, E.; Heusdens, B.; Destiné, J. Evaluation of Aerosol Jet Printing (Ajp) Technology for Electronic Packaging and Interconnect Technique. *2012 4th Electronic System-Integration Technology Conference*; IEEE, 2012; pp 1−5.
(35) Verheecke, W.; Van Dyck, M.; Vogeler, F.; Voet, A.; Valkenaers, H. *Optimizing Aerosol Jet Printing of Silver Interconnects on Polyimide Film for Embedded Electronics Applications*; Eighth International DAAAM Baltic Conference Industrial Engineering: Tallinn, Estonia, Apr 2012; pp 19−21.
(36) Kwon, Y. T.; Lee, Y.; Berkmen, G. K.; Lim, H. R.; Scorr, L.; Jinnah, H. A.; Yeo, W. H. Soft Material-Enabled, Active Wireless, Thin-Film Bioelectronics for Quantitative Diagnostics of Cervical Dystonia. *Adv. Mater. Technol.* **2019**, *4*, 1900458.
(37) Lee, Y.; Nicholls, B.; Lee, D. S.; Chen, Y.; Chun, Y.; Ang, C. S.; Yeo, W.-H. Soft Electronics Enabled Ergonomic Human-Computer Interaction for Swallowing Training. *Sci. Rep.* **2017**, *7*, 46697.
(38) Kim, Y.-S.; Mahmood, M.; Kwon, S.; Herbert, R.; Yeo, W.-H. Robust Human-Machine Interfaces Enabled by a Skin-Like, Electromyogram Sensing System. *Nano-, Bio-, Info-Tech Sensors and 3D Systems III*, International Society for Optics and Photonics, 2019; p 1096903.
(39) Mahmood, M.; Mzurikwao, D.; Kim, Y.-S.; Lee, Y.; Mishra, S.; Herbert, R.; Duarte, A.; Ang, C. S.; Yeo, W.-H. Fully portable and wireless universal brain-machine interfaces enabled by flexible scalp electronics and deep learning algorithm. *Nat. Mach. Intell.* **2019**, *1*, 412−422.
(40) Herboth, T.; Guenther, M.; Fix, A.; Wilde, J. Failure Mechanisms of Sintered Silver Interconnections for Power Electronic Applications. *2013 IEEE 63rd Electronic Components and Technology Conference*; IEEE, 2013; pp 1621−1627.

https://dx.doi.org/10.1021/acsami.0c14193
ACS Appl. Mater. Interfaces 2020, 12, 49398−49406

SUPPORTING INFORMATION

Printed, Wireless, Soft Bioelectronics and Deep Learning Algorithm for Smart Human-Machine Interfaces

Young-Tae Kwon[a]†, Hojoong Kim[a]†, Musa Mahmood[a], Yun-Soung Kim[a], Carl Demolder[a], and Woon-Hong Yeo[a,b,c,]*

[a]George W. Woodruff School of Mechanical Engineering, Institute for Electronics and Nanotechnology, Georgia Institute of Technology, Atlanta, GA 30332, USA.

[b]Wallace H. Coulter Department of Biomedical Engineering, Parker H. Petit Institute for Bioengineering and Biosciences, Georgia Institute of Technology, Atlanta, GA 30332, USA.

[c]Center for Human-Centric Interfaces and Engineering, Neural Engineering Center, Institute for Materials, Institute for Robotics and Intelligent Machines, Georgia Institute of Technology, Atlanta, GA 30332, USA.

†These authors contributed equally.

*Address correspondence to whyeo@gatech.edu

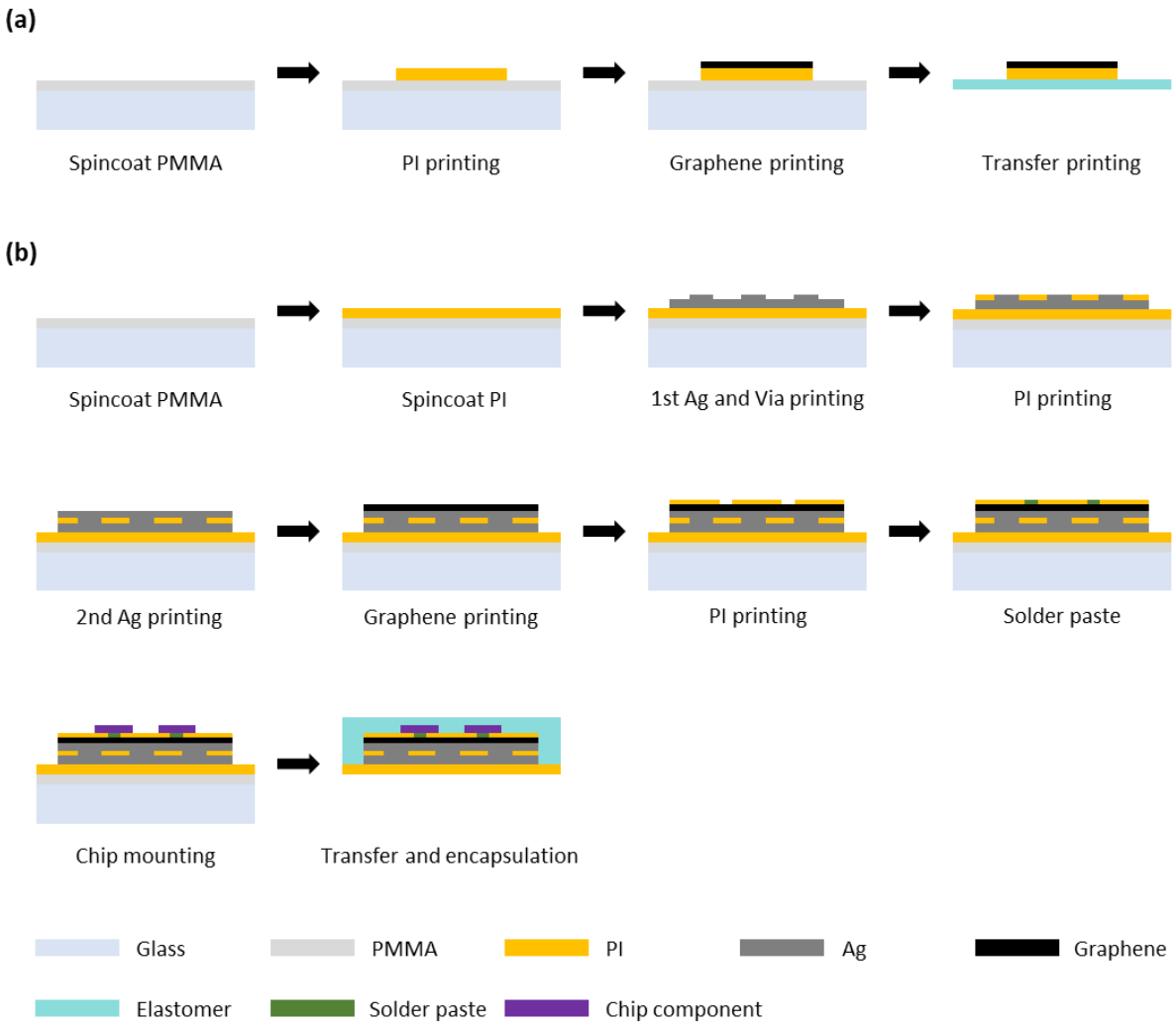

Figure S1. Fabrication of sensors and electronics. (a) Printing of nanomembrane electrodes and transfer printing onto an elastomer substrate. (b) Fabrication of a printed circuit with the integration of chip components.

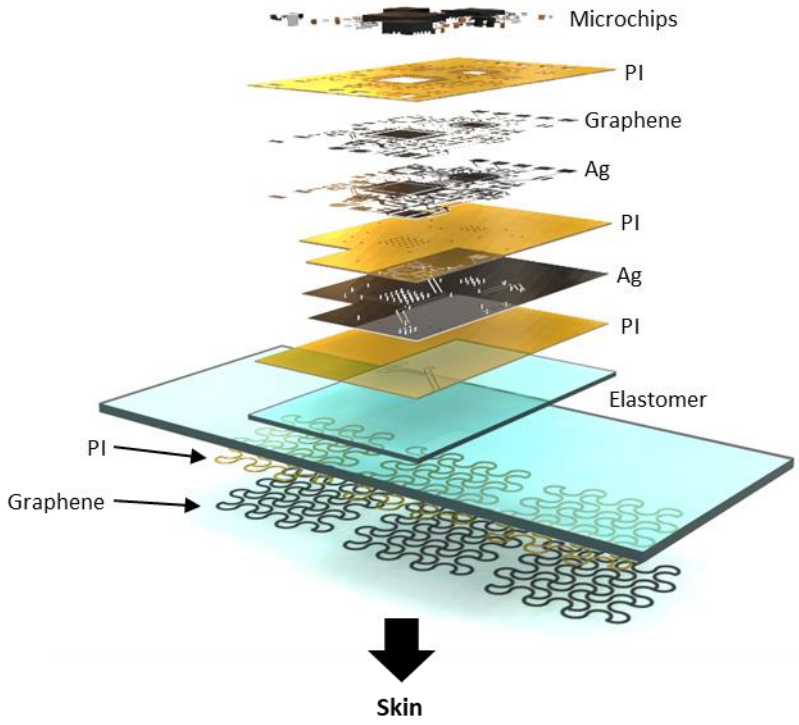

Figure S2. Schematic illustration of multi-layered printed bioelectronics.

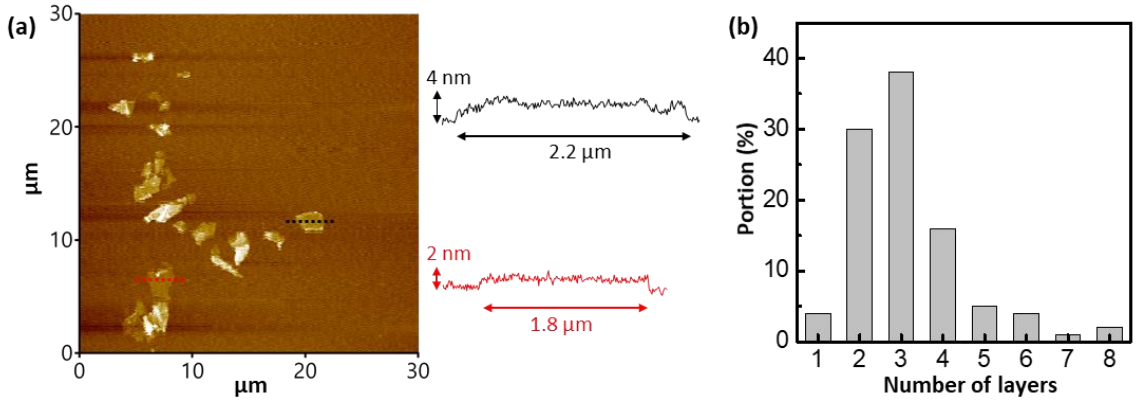

Figure S3. Characterization of graphene dispersed in aqueous ink. (a) AFM image (left) of graphene material dispersed in aqueous ink and two height profiles (right) of the graphene, corresponding to two dotted lines in AFM result. (b) The number of layers of graphene materials. 100 graphene sheets are counted from AFM results.

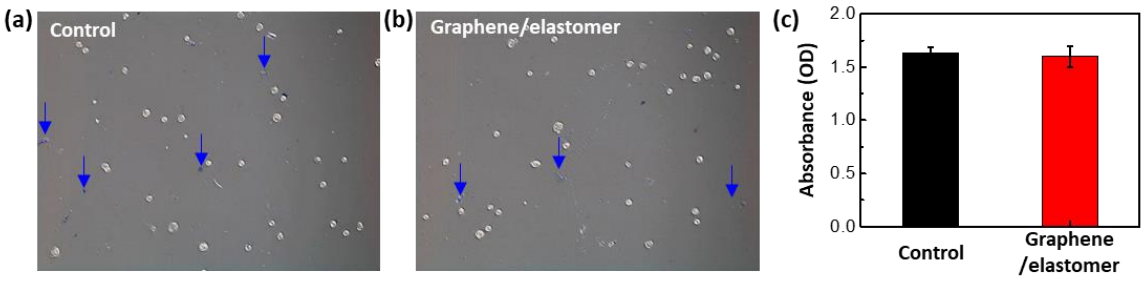

Figure S4. Biocompatibility of printed electrodes. (a,b) Optical microscopic images of cultured keratinocyte cells after exposure to original DMEM (a; control sample) and DMEM with graphene/elastomer (b) after 7 days of culture. In the images, small blue dots represent dead cells (pinpointed by blue arrows). (c) Comparison of cell absorbance of the control and graphene electrode.

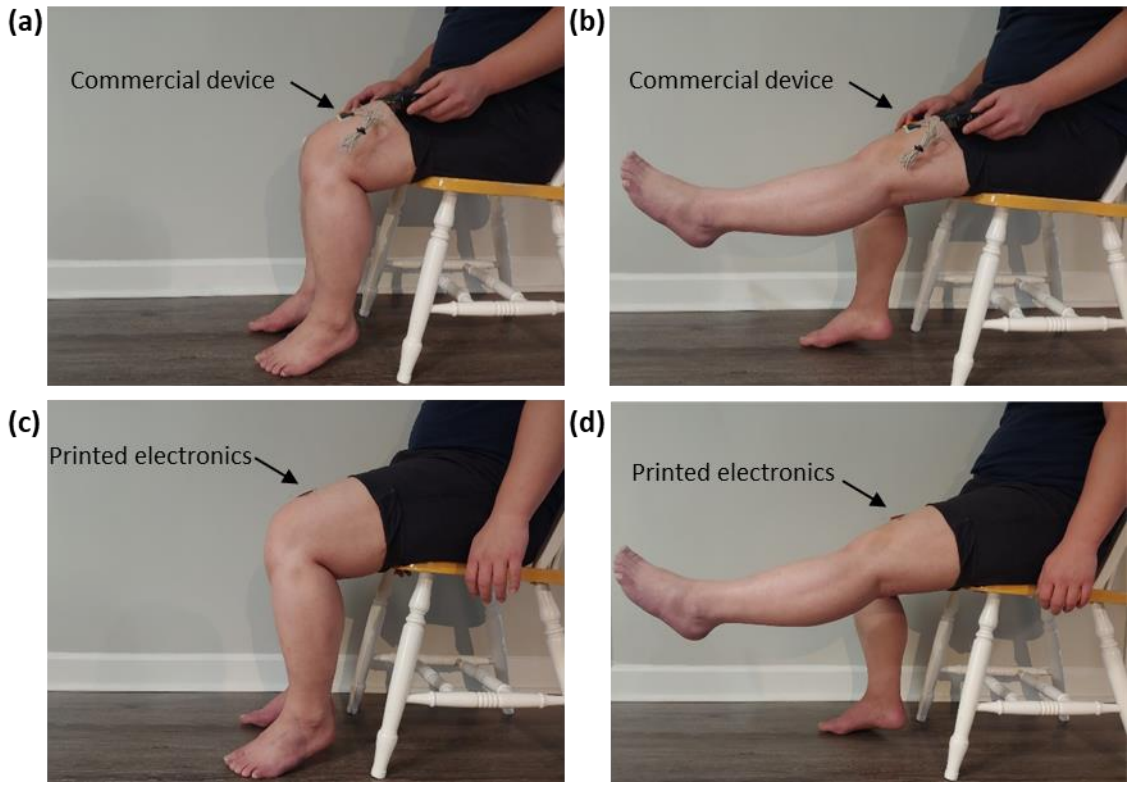

Figure S5. The human leg's gestures mounted with the commercial device and the soft electronics while sitting. (a,b) Photos of rest (a) and leg extension (b) with the commercial device. (c,d) Optical images of rest (c) and leg flexion (d) with the soft electronics. The corresponding EMG signals are shown in Figure 3b and 3d.

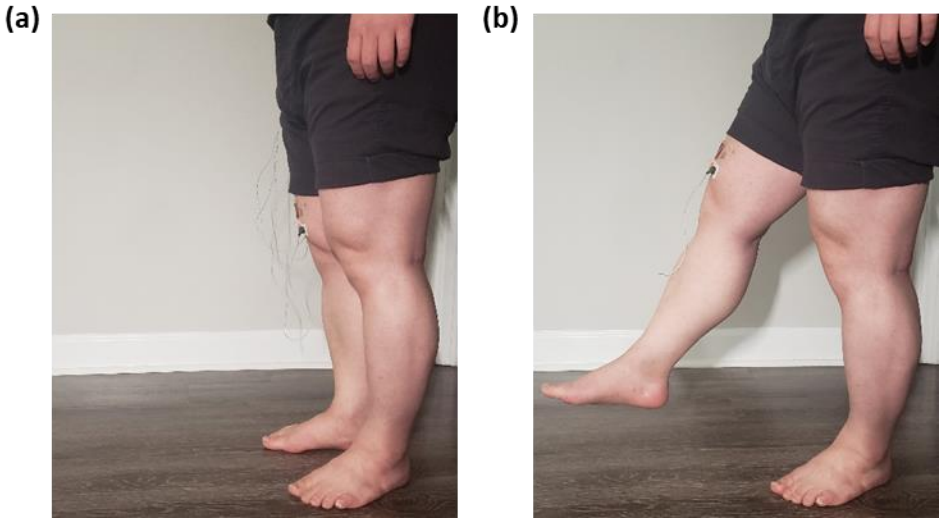

Figure S6. The human leg's gestures mounted with the commercial device and the printed electronics at the same time while standing. (a,b) Photos of still (a) and leg extension (b) with the commercial device and the printed electronics. The corresponding EMG signals are shown in Figure 3h.

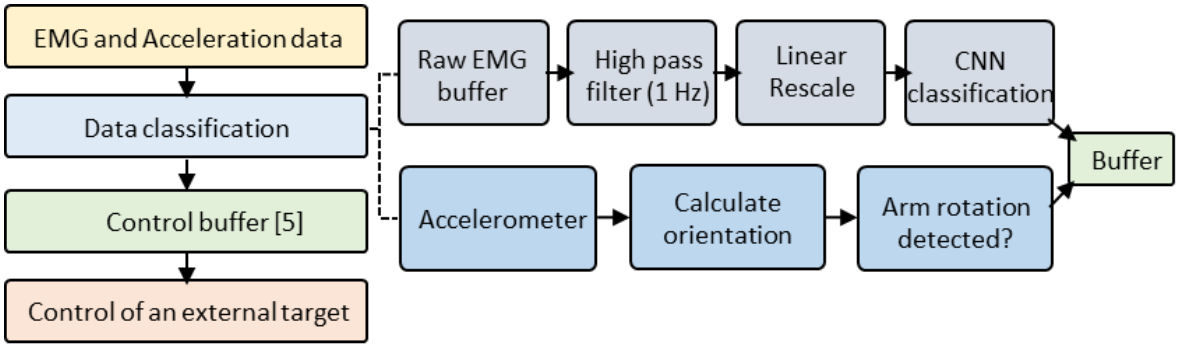

Figure S7. Flowchart showing the overall process from the recording of data (EMG and acceleration) to classification based on machine learning and control of an external target.

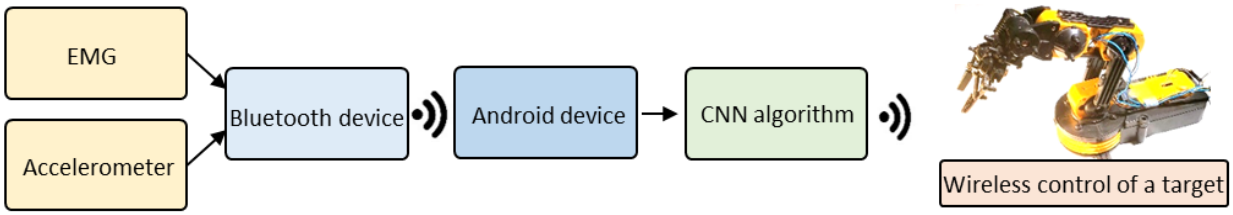

Figure S8. Flowchart showing the sequence from data recording by the wearable bioelectronics to the control of the target.

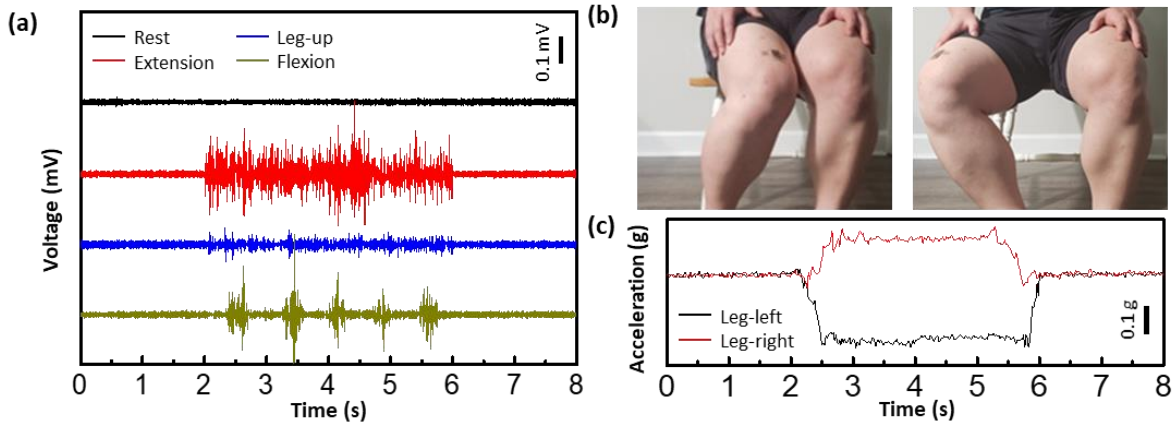

Figure S9. EMG and acceleration data from the human leg's gestures. (a) Representative EMG signals from four different leg gestures, including rest, extension, leg-up, and flexion. and Extension. (b,c) The two gestures, including leg movement left (b, left) and right (b, right), used to control the robotic arm, along with the corresponding acceleration signals in y axis (c).

Table S1. Parameters for ink materials, printing, and curing/sintering. The table shows the details of the condition, including the solvent, viscosity, sheath/atomization rate, nozzle diameter, printing speed, stage temperature, and curing/sintering parameters.

Factor	PI	Ag	Graphene
Solvent (Viscosity)	N-Methyl-2-Pyrrolidone (350 cP)	Ethanol (20 cP)	DI water (6 cP)
Sheath rate (ccm)	20	30	30
Atomization rate (ccm)	1000 (exhaust) 1100 (atomization)	25	40
Nozzle diameter (μm)	300	200	200
Printing speed (mm/s)	10	10	10
Stage temperature (^{o}C)	80	70	70
Post-treatment	Thermal curing (250 ^{o}C, 1 h)	Photonic sintering (2 kV, 2 ms, 5 times)	Thermal treatment (100 ^{o}C, 1 h)

Table S2. List of Commands for controlling the machines. (a) Control of a hand robot via EMG signals from the forearm. (b) Control of a robotic arm via EMG signals from the upper leg.

(a)

Gesture \ Machine	Hand robot
Open	Open
Closed	Closed
Index	Index
Wrist flexion	Middle
Rotate CW	Ring
Rotate CCW	Little

(b)

Gesture \ Machine	Robotic arm
Rest	Still
Extension	Down
Leg-up	Up
Flexion	Grab
Leg-left	Left
Leg-right	Right

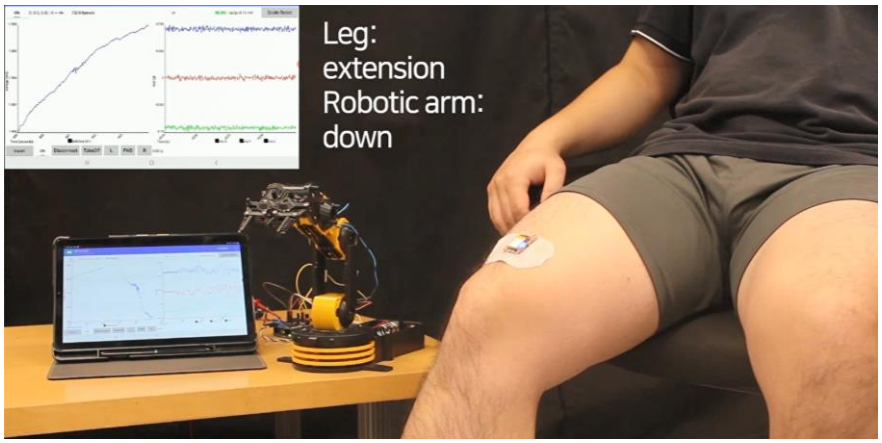

Movie S1. Real-time control of a robotic arm via EMG signals from the upper leg.